AIAA JOURNAL
Vol. 46, No. 11, November 2008

Computation of Shock Cell Structure of Dual-Stream Jets for Noise Prediction

Christopher K. W. Tam* and Nikolai N. Pastouchenko†
Florida State University, Tallahassee, Florida 32306-4510
and
K. Viswanathan‡
The Boeing Company, Seattle, Washington 98124

DOI: 10.2514/1.37045

Broadband shock cell noise is an important component of aircraft interior noise during cruise. At cruise, the secondary jet of most modern day jet engines is supersonic. As a result, a shock cell structure develops in the jet plume. The interaction of large turbulence structures of the jet flow and the periodic components of the shock cells results in the emission of highly directional broadband shock cell noise. The primary objective of this investigation is to develop a computational method to calculate the shock cell structures of dual-stream jets issued from separate flow nozzles. Computation of the Fourier modes of such shock cell structures is also considered. Based on the dominant wave numbers computed by the method developed, the frequencies at the peaks of broadband shock cell noise spectra at various radiation directions are calculated. Good agreements are found with experimental measurements over a wide range of primary and secondary jet Mach numbers. The good agreements provide a validation of the accuracy of the computation method.

I. Introduction

AT CRUISE condition, the Mach number of the secondary jet of a commercial jet engine with a dual-stream nozzle would, generally, be supersonic. At the same time, the hot primary jet would be operating at a high subsonic Mach number. A shock cell structure would, therefore, form in the plume of the secondary jet. The presence of shock cells, inevitably, leads to the generation of broadband shock cell noise. Because of the proximity of the engine to the aircraft body, the noise emitted will impinge on its fuselage. When transmitted into the aircraft, it contributes significantly to cabin interior noise.

Interest in broadband shock cell noise began with the pioneering work of Harper-Bourne and Fisher [1]. During the ensuing years, there have been a substantial number of publications in the literature on broadband shock cell noise from single-stream jets [2–13]. These studies investigated the noise generation mechanisms, the near- and far-field noise characteristics, jet temperature, and forward flight effects. Semi-empirical noise spectrum and intensity prediction methods and scaling formulas were also developed. Recently, there is a renewed interest in broadband shock cell noise. These investigations [14–16] made use of the advances in computational methods to try to predict the noise in the far field numerically. Most of the preceding referenced investigations are motivated by community noise consideration. More recent interest on this subject centers on broadband shock cell noise as a source of cabin noise during cruise. At the present time, most commercial jet engines use dual-stream separate flow nozzles. There are now a number of investigations on broadband shock cell noise from dual-stream jets including forward flight effects at cruise condition [17–21]. Some of these investigations concentrate on fundamental issues relating to the shock cells, the noise characteristics, and jet operating conditions for minimum noise. There are also studies of the effect of chevrons on this noise component [22–24]. The effect of chevrons on jet mixing noise is still not well understood. The same is true with broadband shock cell noise.

For a jet from a separate flow nozzle without a center plug, there are two basic shock cell systems. One shock cell structure is initiated at the nozzle exit of the secondary jet. This is the result of pressure mismatch between that in the jet at the nozzle exit and the ambient pressure. The other shock cell structure is initiated at the nozzle exit plane of the primary jet. At this location, the secondary jet starts to merge with the primary jet. But the flow directions of the two jets are not parallel to each other. Thus, the merging process requires the secondary jet to turn a small angle. It is well known in gas dynamics that the turning of a supersonic stream would lead to the formation of a shock. The shock is trapped inside the secondary jet bouncing between the outside mixing layer and the internal shear layer separating the primary and the secondary jet. In this way, a second shock cell structure is formed.

It is widely recognized that broadband shock cell noise from single-stream supersonic jets is generated by the interaction of the large turbulence structures of the jet flow and the shock cells as the former move downstream through the latter. The interaction is quite coherent, which leads to fairly directional radiation with preference in the forward and sideline directions. The directional characteristics of shock cell noise are, to a large extent, influenced by the quasi periodicity of the shock cell structure. This structure can be decomposed into Fourier modes. The interaction of the large turbulence structures of the jet flow and the shock cells may, therefore, be considered as interactions with the different Fourier modes. The Fourier modes are not exactly harmonics of the fundamental. This is because the shock cell structure is not precisely spatially periodic. In a shock cell noise spectrum, several peaks can be identified. Each of these peaks represents the interaction of the large turbulence structures with a single Fourier mode of the shock cells. The dominant peak is, invariably, generated by the first or the fundamental mode. Contributions from the high-order Fourier modes generally decrease rapidly as the mode number increases.

Presented as Paper 0027 at the 46th AIAA Aerospace Sciences Meeting and Exhibit, Reno, NV, 7–10 January 2008; received 7 February 2008; revision received 17 June 2008; accepted for publication 23 June 2008.

*Robert O. Lawton Distinguished Professor, Department of Mathematics. Fellow AIAA.
†Research Associate, Department of Mathematics. Member AIAA.
‡Associate Technical Fellow, Aeroacoustics and Fluid Mechanics. Associate Fellow AIAA.

The objective of this investigation is to develop a computational model and prediction method for computing the shock cells of dual-stream jets from separate flow nozzles. The present investigation concentrates on static jets. The more important but also more complex cases involving forward flight at cruise will be deferred to a future study. Tam et al. [25] have shown that, for single-stream jets with weak shocks, a linear shock cell structure model would be capable of providing fairly accurate predictions of the principal characteristics of the shock cells. In their work, the Fourier modes were computed by a multiple-scales expansion method. These modes were then added together to form a shock cell structure. They demonstrated that the computed shock cell spacing, amplitude, and detailed features compared well with the experimental measurements of Norum and Seiner [4]. In the present investigation, a similar linear shock cell model is used. Unlike the work of Tam et al. [25], however, an advanced computational aeroacoustics method is used to compute the shock cell structure directly from the governing equations. Specifically, the dispersion-relation-preserving (DRP) scheme is used to time march the shock cell solution on a well-designed grid to a time-independent state. A somewhat different formulation is developed for the purpose of computing the individual Fourier modes of the shock cell structure. This approach is entirely new and is applicable to the shock cell system initiated at the secondary jet exit or the shock cell system created by the turning of the supersonic flow by the primary jet. To validate the accuracy of the computation, the predicted shock noise frequencies at the spectrum peaks at various directions of radiation are compared with experimental measurements. Good agreements are found.

II. Linear Shock Cell Model

We consider the shock cells of dual-stream jets from separate flow nozzles without a center plug. Figure 1 shows a schematic diagram of the nozzle cross section. A companion experimental program to the present computational effort is carried out at The Boeing Company. In the experiment, the dimensions of the nozzle are

$$H = 3 \text{ in.}, \qquad W = 5.68 \text{ in.}, \qquad D_p = 2.45 \text{ in.}$$
$$h = 0.879 \text{ in.}, \qquad \alpha = 8.95 \deg$$

At cruise condition, the secondary jet is supersonic, whereas the primary jet is high subsonic. Thus, a shock cell structure develops in the plume of the secondary jet. For the nozzle geometry under consideration, there are two shock cell structures. The dominant shock cells are the result of pressure mismatch at the nozzle exit of the secondary jet. Figure 2 shows a sketch of such a shock cell system.

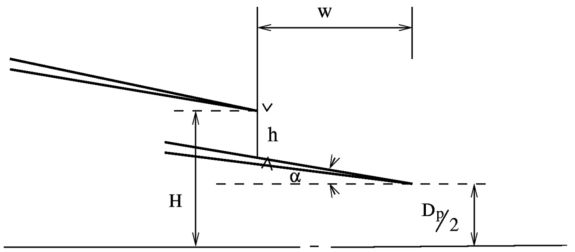

Fig. 1 Cross section of dual-stream separate flow nozzle without a center plug.

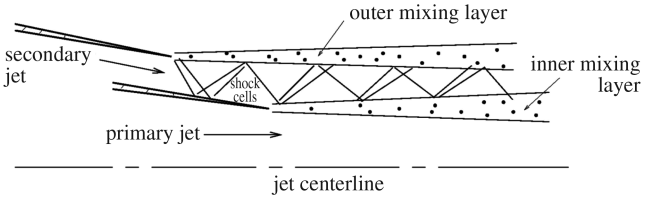

Fig. 2 Schematic diagram of shock cell structure initiated by pressure mismatch at the secondary nozzle exit.

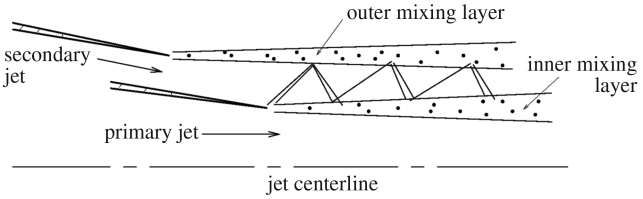

Fig. 3 Schematic diagram of shock cell structure initiated by flow turning at the exit of the primary jet.

With a nozzle configuration given in Fig. 1, the supersonic secondary jet impinges on the primary jet at an angle at the exit of the primary jet nozzle. This causes the jet fluid to turn. It is well known that the turning of a supersonic flow leads to the formation of a shock. For the nozzle geometry given in Fig. 1, the shock is initiated near the lip of the primary nozzle. The repeated reflection of the shocks and expansion fans by the outer and inner mixing layer of the jet forms a second shock cell system as illustrated in Fig. 3. The results of the present investigation, however, indicates that, for a small turning angle α (less than 10 deg), the shock cell system due to flow turning is weak compared to the pressure mismatch shock cell system. Therefore, in this paper, our concern is primarily with the shock cell structure starting at the lip of the secondary nozzle.

Jet engine design does not allow the presence of strong shocks in the jet plume. For weak shocks, Tam et al. [25] have demonstrated that the use of a linear shock cell model could provide shock cell predictions that compared well with experimental measurements. Here, we will adopt a linear model for computing the shock cell structures in the plume of the dual-stream jets. In the linear model, the shock structure is regarded as compressible disturbances superposed on the mean flow of the jet. The mean flow in this case is a perfectly expanded jet with static pressure at the nozzle exit of the secondary jet equal to ambient pressure. In this investigation, such a mean flow is computed by the Florida State University Parabolized Code. Details of the mathematical basis and computational algorithm of the code can be found in the work of Tam and Pastouchenko [26]. In [26], it is shown that the computed mean flow profiles of dual-stream jets from separate flow nozzles with a center plug agree well with experimental measurements.

A. Shock Cell Starting Conditions at the Nozzle Exit of the Secondary Jet

In calculating the mean flow, the secondary jet is assumed to be perfectly expanded. This means that the pressure of the jet at the nozzle exit is equal to ambient pressure. For a supersonic jet issued from a convergent nozzle, this is incorrect. The jet is choked and the Mach number at the nozzle exit is unity. The exit pressure of the jet is determined by this choking condition. Thus, the exit pressure is not equal to ambient pressure. This pressure mismatch is what leads to the formation of shock cells.

Several sets of variables will be involved in determining the shock cell starting conditions at the nozzle exit of the secondary jet. For clarity, the following notations will be used. Subscript s denotes a variable of the secondary jet. Subscript p denotes a variable of the primary jet. Subscript a denotes an ambient variable. Superscript r denotes a variable in reservoir condition. Superscript e denotes a variable at the nozzle exit. Variables without a superscript are fully expanded physical quantities, for example, M_s and M_p are the Mach numbers of the secondary and primary jets.

Conservation of enthalpy in the jet flow leads to the following equation:

$$c_p T_s^{(r)} = c_p T_s^{(e)} + \tfrac{1}{2}(u_s^{(e)})^2 = c_p T_s + \tfrac{1}{2}u_s^2 \tag{1}$$

It will be assumed that the nozzle flow is isentropic. On combining with Eq. (1), the following relationships can be easily established:

$$\frac{T_s^{(r)}}{T_s^{(e)}} = 1 + \frac{\gamma - 1}{2}(M_s^{(e)})^2 = \frac{\gamma + 1}{2} = \left(\frac{p_s^{(r)}}{p_s^{(e)}}\right)^{\frac{\gamma-1}{\gamma}} \tag{2}$$

$$\frac{p_s^{(r)}}{p_a} = \left(1 + \frac{\gamma - 1}{2} M_s^2\right)^{\frac{\gamma}{\gamma - 1}} \tag{3}$$

Thus,

$$\frac{p_s^{(e)}}{p_a} = \left[\frac{2}{\gamma + 1}\left(1 + \frac{\gamma - 1}{2} M_s^2\right)\right]^{\frac{\gamma}{\gamma - 1}} \tag{4}$$

Let $\Delta p_s^{(e)}$ be the pressure mismatch to be imposed at the exit of the secondary nozzle in the linear shock cell model. In dimensionless form, $\Delta p_s^{(e)}$ is given by

$$\frac{\Delta p_s^{(e)}}{\rho_p u_p^2} \equiv \frac{p_s^{(e)} - p_a}{\rho_p u_p^2} = \left(\frac{p_s^{(e)}}{p_a} - 1\right) \frac{1}{\gamma M_p^2} \tag{5}$$

Upon using Eq. (4), it is found

$$\frac{\Delta p_s^{(e)}}{\rho_p u_p^2} = \left\{\left[\frac{2}{\gamma + 1}\left(1 + \frac{\gamma - 1}{2} M_s^2\right)\right]^{\frac{\gamma}{\gamma - 1}} - 1\right\} \frac{1}{\gamma M_p^2} \tag{6}$$

Similarly, it is straightforward to find that the velocity mismatch at the exit of the secondary jet for the linear shock cell model is given by

$$\frac{\Delta u_s^{(e)}}{u_p} = \left[\frac{1}{M_s}\left(\frac{2}{\gamma + 1}\right)^{\frac{1}{2}}\left(1 + \frac{\gamma - 1}{2} M_s^2\right)^{\frac{1}{2}} - 1\right] \times \frac{M_s}{M_p}\left[\frac{1 + \frac{1}{2}(\gamma - 1) M_p^2}{1 + \frac{1}{2}(\gamma - 1) M_s^2}\right]^{\frac{1}{2}}\left(\frac{T_a}{T_p^{(r)}}\right)^{\frac{1}{2}} \tag{7}$$

In deriving Eq. (7), the reservoir temperature of the secondary jet has been assumed to be equal to ambient temperature. This is true for most commercial jet engines.

B. Governing Equations

The governing equations for the linear shock cell model are the linearized Reynolds-averaged Navier–Stokes equations (RANS). To simplify the computation, we will invoke the locally parallel flow approximation. The nonparallel flow effects are generally small and will be insignificant for broadband shock cell noise consideration. With respect to D_p (diameter of the primary jet) as length scale, u_p (fully expanded velocity of the primary jet) as the velocity scale, D_p/u_p as the time scale, ρ_p (fully expanded gas density of the primary jet) as the density scale, $\rho_p u_p^2$ as the pressure scale, the governing equations (momentum and energy equations) in cylindrical coordinates (r, ϕ, x) are

$$\frac{\partial v}{\partial t} + \bar{u}\frac{\partial v}{\partial x} = -\frac{1}{\bar{\rho}}\frac{\partial p}{\partial x} + \frac{1}{R}\left(\nabla^2 v - \frac{v}{r^2}\right) \tag{8}$$

$$\frac{\partial u}{\partial t} + \bar{u}\frac{\partial u}{\partial x} + v\frac{\partial \bar{u}}{\partial r} = -\frac{1}{\bar{\rho}}\frac{\partial p}{\partial x} + \frac{1}{R}\nabla^2 u \tag{9}$$

$$\frac{\partial p}{\partial t} + \bar{u}\frac{\partial p}{\partial x} + \frac{1}{M_p^2}\left(\frac{\partial v}{\partial r} + \frac{v}{r} + \frac{\partial u}{\partial x}\right) = 0 \tag{10}$$

where $\bar{u}$, $\bar{\rho}$, and $\bar{p}$ are the mean flow velocity, density, and pressure, $R = \bar{u}_p D_p/\nu_t$ is the turbulent Reynolds number, and ν_t is the turbulent viscosity. In this work, ν_t is taken to be the value given by the k-ε model from the mean flow calculation. This value is similar to the value used by Tam et al. [25]. Equation (10) is the linearized energy equation for an inviscid non-heat-conducting gas.

III. Computation of Shock Cell Structure

A. Oblique Cartesian Coordinates

In the region between the exit plane of the secondary nozzle and that of the primary nozzle, the natural coordinate system to use is the oblique Cartesian coordinates (ξ, η), as shown in Fig. 4. The oblique Cartesian coordinate mesh forms a body-fitted grid for the separate flow nozzle. These coordinates (ξ, η) are related to the cylindrical coordinates (r, x) by

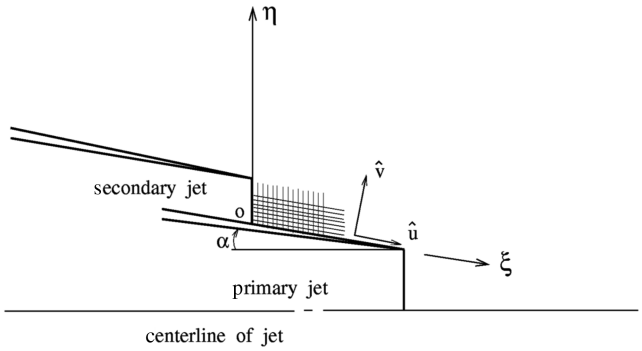

Fig. 4 Oblique Cartesian coordinate system.

$$x = \xi\cos\alpha + x_0 \qquad r = \eta - \xi\sin\alpha + r_0 \tag{11}$$

where (r_0, x_0) are the coordinates of the origin of the oblique Cartesian coordinates.

To facilitate the enforcement of a boundary condition at the nozzle wall, a change of dependent variables from (u, v) to $(\hat{u}, \hat{v})$, as shown in Fig. 4, is implemented. The variables $(\hat{u}, \hat{v})$ are related to (u, v) by

$$\hat{u} = u\cos\alpha - v\sin\alpha \qquad \hat{v} = u\sin\alpha + v\cos\alpha \tag{12}$$

On applying a change of variable from (u, v) to $(\hat{u}, \hat{v})$ and from (r, x) to (ξ, η), it is easy to show that governing Eqs. (8–10) become

$$\frac{\partial \hat{u}}{\partial t} = -\bar{u}\left(\frac{1}{\cos\alpha}\frac{\partial \hat{u}}{\partial \xi} + \tan\alpha\frac{\partial \hat{u}}{\partial \eta}\right) + \frac{\partial \bar{u}}{\partial r}\cos\alpha(\hat{u}\sin\alpha - \hat{v}\cos\alpha) - \frac{1}{\bar{\rho}}\frac{\partial p}{\partial \xi} + \frac{1}{R}\left(\frac{1}{\cos^2\alpha}\frac{\partial^2 \hat{u}}{\partial \eta^2} + \frac{1}{r}\frac{\partial \hat{u}}{\partial \eta} + \frac{1}{\cos^2\alpha}\frac{\partial^2 \hat{u}}{\partial \xi^2} + \frac{2\sin\alpha}{\cos^2\alpha}\frac{\partial^2 \hat{u}}{\partial \xi \partial \eta} - \frac{\sin\alpha(\hat{u}\sin\alpha - \hat{v}\cos\alpha)}{r^2}\right) \tag{13}$$

$$\frac{\partial \hat{v}}{\partial t} = -\bar{u}\left(\frac{1}{\cos\alpha}\frac{\partial \hat{v}}{\partial \xi} + \tan\alpha\frac{\partial \hat{v}}{\partial \eta}\right) + \frac{\partial \bar{u}}{\partial r}\sin\alpha(\hat{u}\sin\alpha - \hat{v}\cos\alpha) - \frac{1}{\bar{\rho}}\left(\frac{1}{\cos\alpha}\frac{\partial p}{\partial \eta} + \tan\alpha\frac{\partial p}{\partial \xi}\right) + \frac{1}{R}\left(\frac{1}{\cos^2\alpha}\frac{\partial^2 \hat{v}}{\partial \eta^2} + \frac{1}{r}\frac{\partial \hat{v}}{\partial \eta} + \frac{1}{\cos^2\alpha}\frac{\partial^2 \hat{v}}{\partial \xi^2} + \frac{2\sin\alpha}{\cos^2\alpha}\frac{\partial^2 \hat{v}}{\partial \xi \partial \eta} + \frac{\cos\alpha(\hat{u}\sin\alpha - \hat{v}\cos\alpha)}{r^2}\right) \tag{14}$$

$$\frac{\partial p}{\partial t} = -\bar{u}\left(\frac{1}{\cos\alpha}\frac{\partial p}{\partial \xi} + \tan\alpha\frac{\partial p}{\partial \eta}\right) - \frac{1}{M_p^2}\left(\frac{1}{\cos\alpha}\frac{\partial \hat{v}}{\partial \eta} + \frac{\partial \hat{u}}{\partial \xi} + \tan\alpha\frac{\partial \hat{v}}{\partial \xi} - \frac{\hat{u}\sin\alpha - \hat{v}\cos\alpha}{r}\right) \tag{15}$$

In the present study, the preceding three equations are used to compute the shock cell structure in the oblique Cartesian coordinates region of the computational domain.

B. Mesh Design and Computation Algorithm

It cannot be overemphasized that a good mesh design is essential to an accurate and successful computation. Figure 5 shows the computation domain we use in the present investigation. The shock cell structure exists only in the supersonic region of the secondary jet. By means of our mean flow code, we are able to establish, for the jet operating parameters in which we are interested, that the supersonic core terminates well within 20 primary nozzle diameters

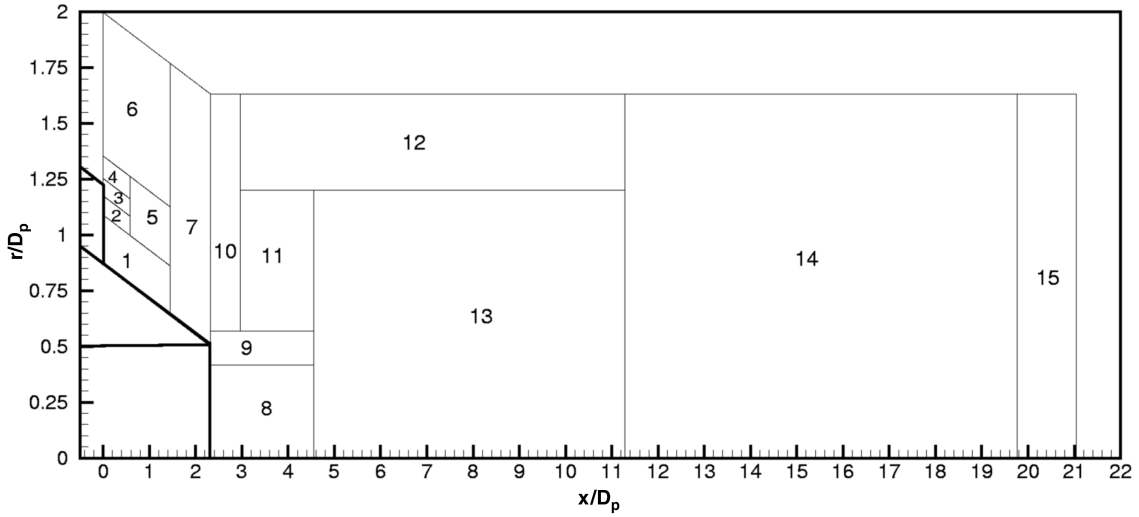

Fig. 5 Computation domain and its partition into 15 subdomains.

downstream. Radially, the shock cells are confined to the jet flow. Thus, extending the computation domain from the jet axis to slightly beyond 1.5 D_p is quite adequate for shock cell computation.

The computation strategy is to start with a zero solution. At time $t = 0$, the pressure and velocity mismatch conditions, Eqs. (6) and (7), are imposed at the exit of the secondary nozzle. To avoid introducing an excessive amount of high wave number disturbances into the computation domain, the mismatched values are raised slowly to their full values over a short period of time. The numerical solution is marched in time until a steady-state solution is reached. The seven-point stencil multi-mesh-size multi-time-step DRP scheme [27,28] is used as the computation algorithm. This scheme has the significant advantage of allowing a user to use different size mesh in different parts of the computation domain. For the present shock cell problem, the computation domain is divided into 15 subdomains (see Fig. 5). The mesh size of a neighboring subdomain may change by a factor of 2. Table 1 shows the mesh size distribution in the 15 subdomains. The finest meshes are concentrated in the thin shear layer region just downstream of the nozzle exit. The mesh size increases in the downstream direction. In designing the mesh, special effort is made to maintain the aspect ratio of the grid to be close to unity. The total number of mesh points is approximately 400,000.

The DRP scheme, unlike most computational algorithms, uses a four-level time marching algorithm. This allows the scheme to employ different time steps in neighboring subdomains whenever there is a change in mesh size. Thus, in the computation code, with a change in mesh size between adjacent subdomains, there is a corresponding change in the size of the time step. This maintains numerical stability and, at the same time, makes the computation extremely efficient. In running the computer code, most of the computations are concentrated in the fine mesh subdomains. Mesh points in the coarse mesh subdomains are updated only occasionally. Mesh-size-change interfaces are often sources of spurious short waves. To suppress the generation, and for the purpose of damping out these spurious waves after they are inadvertently generated, artificial selective damping is incorporated in the computation scheme. Addition of artificial selective damping appears to work very well, as we have not encountered any problem with grid-to-grid oscillations and other spurious short waves.

Table 1 Mesh size distribution

Subdomain	$\Delta\xi$ or Δx	$\Delta\eta$ or Δr	Time step
1	$4\Delta\xi$	$4\Delta\eta$	$4\Delta t$
2	$2\Delta\xi$	$2\Delta\eta$	$2\Delta t$
3	$\Delta\xi$	$\Delta\eta$	Δt
4	$2\Delta\xi$	$2\Delta\eta$	$2\Delta t$
5	$2\Delta\xi$	$2\Delta\eta$	$2\Delta t$
6	$4\Delta\xi$	$4\Delta\eta$	$4\Delta t$
7	$4\Delta\xi$	$4\Delta\eta$	$4\Delta t$
8	$2\Delta x$	$2\Delta r$	$4\Delta t$
9	Δx	Δr	$2\Delta t$
10	$2\Delta x$	$2\Delta\eta$	$4\Delta t$
11	$2\Delta x$	$2\Delta r$	$4\Delta t$
12	$4\Delta x$	$4\Delta r$	$8\Delta t$
13	$2\Delta x$	$2\Delta r$	$4\Delta t$
14	$4\Delta x$	$4\Delta r$	$8\Delta t$
15	$8\Delta x$	$8\Delta r$	$16\Delta t$
$\Delta\xi = 0.0015$, $\Delta x = 0.004$, $\Delta\eta = 0.0014$, $\Delta r = 0.004$, $\Delta t = 0.00023$			

Outside the supersonic flow region, the disturbances associated with the shock cells decay exponentially. They should be nearly equal to zero at the edge of the computational domain. However, to minimize any possible reflection from the external computational boundaries, a damping region is incorporated along the entire boundary. In the damping region, an artificial damping term is added to each of the governing equations. This provides a time damping to the numerical solution in this region. At the nozzle exit region of the primary jet, there is no pressure and velocity mismatch, as the primary jet is subsonic. A damping region is added on the left side of the nozzle exit, again for the purpose of minimizing reflection.

Recall that turbulent viscosity terms are added to Eqs. (8–10). The purpose of these terms is to simulate the effect of turbulence in the mixing layers of the jet. These terms are unnecessary outside the mixing layers. In the present computation, they are neglected in the lower part of subdomains 1 and 7 adjacent to the nozzle wall and in the lower part of subdomains 8, 13, 14, and 15 adjacent to the axis of the primary jet. Effectively, the inviscid equations are applied to these regions.

To complete the specification of boundary conditions used in the computation, we would like to mention that the wall boundary conditions formulated by Tam and Dong [29] is used at the wall between the nozzle exits of the secondary and primary jet. At the jet axis ($r \to 0$), the governing equations, written in cylindrical coordinates, have an apparent singularity. To avoid this complication computationally, a jet axis boundary condition had been developed by Shen and Tam [30]. Here, the problem is axisymmetric. Implementation of the axisymmetric jet axis boundary condition is quite straightforward.

IV. Fourier Modes of a Shock Cell Structure

In the case of a supersonic jet bounded by a vortex sheet, Pack [31] found an analytical solution for the shock cell structure. The solution is in the form of a series expansion in terms of the eigen- or Fourier modes of the jet flow. Tam et al. [25] extended this solution to jets with a finite thickness mixing layer by using the method of multiple scales. There are inherent advantages as well in constructing the shock cell solution in terms of the Fourier modes. Tam [10,11]

observed that a Fourier mode is spatially quasi periodic. He proposed that the passage of large turbulence structures of the jet flow through a Fourier mode would lead to coherent periodic scattering resulting in strong directional acoustic radiation. The radiated sound is the broadband shock cell noise. His theory, based on this noise generation mechanism, has proven capable of predicting broadband shock cell noise spectra and near-field pressure contours that match well with experimental measurements. Earlier, Tam and Tanna [3] considered the coherent interaction of large turbulence structures, represented by traveling waves, and the jth Fourier mode of a shock cell structure. They derived a mathematical relation between the frequency at the peak of the noise spectrum f_j and the direction of radiation θ (inlet angle) in the form (see also Tam et al. [9]):

$$f_j = \frac{u_c k_j}{2\pi(1 + M_c \cos\theta)}, \qquad j = 1, 2, 3, \ldots \tag{16}$$

where u_c is the convection velocity of the large turbulence structures, $M_c = u_c/a_\infty$ is the convective Mach number, and k_j is the wave number of the jth Fourier mode of the shock cell structure. The derivation of Eq. (16) is not restricted to single-stream supersonic jets. Thus, we expect Eq. (16) to be applicable to dual-stream jets as well.

A. Shock Cell Fourier Modes: Starting Conditions

Shock cell Fourier modes satisfy the same governing equations as the shock cell structure. Therefore, to compute each Fourier mode, Eqs. (13–15) will again be used. The only difference between the two calculations is the starting conditions at the nozzle exit of the secondary jet.

We will now consider the appropriate starting conditions for computing the Fourier modes. By Eq. (11), the oblique Cartesian coordinates and the cylindrical coordinates are related by

$$r = r_0 + \eta - \tan\alpha(x - x_0) \tag{17}$$

For practical jet engine design, the angle α is very small. Hence, near the nozzle exit of the secondary jet, where x is nearly equal to x_0, a good approximation is to replace $1/r$ by $1/(\eta + r_0)$. Now, let $\varsigma = (\eta + r_0)$, then $\partial/\partial\eta$ becomes $\partial/\partial\varsigma$. We will use an inviscid model for determining the Fourier mode starting conditions. On neglecting the time-dependent and turbulent viscosity terms, governing Eqs. (13–15) become,

$$-\frac{\bar{u}}{\cos\alpha}\left(\frac{\partial\hat{u}}{\partial\xi} + \sin\alpha\frac{\partial\hat{u}}{\partial\varsigma}\right) + \frac{\partial\bar{u}}{\partial r}\cos\alpha(\hat{u}\sin\alpha - \hat{v}\cos\alpha) - \frac{1}{\bar{\rho}}\frac{\partial p}{\partial\xi} = 0 \tag{18}$$

$$-\frac{\bar{u}}{\cos\alpha}\left(\frac{\partial\hat{v}}{\partial\xi} + \sin\alpha\frac{\partial\hat{v}}{\partial\varsigma}\right) + \frac{\partial\bar{u}}{\partial r}\sin\alpha(\hat{u}\sin\alpha - \hat{v}\cos\alpha) - \frac{1}{\bar{\rho}}\left(\frac{1}{\cos\alpha}\frac{\partial p}{\partial\varsigma} + \tan\alpha\frac{\partial p}{\partial\xi}\right) = 0 \tag{19}$$

$$\frac{\bar{u}}{\cos\alpha}\left(\frac{\partial p}{\partial\xi} + \sin\alpha\frac{\partial p}{\partial\varsigma}\right) + \frac{1}{M_p^2}\left(\frac{1}{\cos\alpha}\frac{\partial\hat{v}}{\partial\varsigma} + \frac{\partial\hat{u}}{\partial\xi} + \tan\alpha\frac{\partial\hat{v}}{\partial\xi} - \frac{\hat{u}\sin\alpha - \hat{v}\cos\alpha}{\varsigma}\right) = 0 \tag{20}$$

We will now look for Fourier mode solutions of Eqs. (18–20) in the form of a series expansion in α. Let

$$\begin{bmatrix}\hat{u}\\ \hat{v}\\ p\end{bmatrix} = Re\left\{\begin{bmatrix}\tilde{u}(\varsigma)\\ \tilde{v}(\varsigma)\\ p(\varsigma)\end{bmatrix}e^{ik\xi}\right\} \tag{21}$$

where k is the wave number. Here, k and the amplitude vector are expanded as a power series in α. That is,

$$k = k_0 + \alpha k_1 + \alpha^2 k_2 + \alpha^3 k_3 + \cdots \tag{22}$$

$$\begin{bmatrix}\tilde{u}\\ \tilde{v}\\ \tilde{p}\end{bmatrix} = \begin{bmatrix}\tilde{u}_0\\ \tilde{v}_0\\ \tilde{p}_0\end{bmatrix} + \alpha\begin{bmatrix}\tilde{u}_1\\ \tilde{v}_1\\ \tilde{p}_1\end{bmatrix} + \alpha^2\begin{bmatrix}\tilde{u}_2\\ \tilde{v}_2\\ \tilde{p}_2\end{bmatrix} + \cdots \tag{23}$$

Substitution of Eqs. (21–23) into Eqs. (18–20) and partitioning terms according to powers of α, it is straightforward to find that the lowest order terms satisfy the following system of equations:

$$ik_0\bar{u}\tilde{u}_0 + \frac{\partial\bar{u}}{\partial r}\tilde{v}_0 + \frac{ik_0}{\bar{\rho}}\tilde{p}_0 = 0 \tag{24}$$

$$ik_0\bar{u}\tilde{v}_0 + \frac{1}{\bar{\rho}}\frac{d\tilde{p}_0}{d\varsigma} = 0 \tag{25}$$

$$ik_0\bar{u}\tilde{p}_0 + \frac{1}{M_p^2}\left(\frac{d\tilde{v}_0}{d\varsigma} + ik_0\tilde{u}_0 + \frac{\tilde{v}_0}{\varsigma}\right) = 0 \tag{26}$$

In this work, we will limit our attention only to the lowest order terms.

B. Eigenvalues and Eigenfunctions

Equations (24–26) form a first-order differential system. We may simplify the system by eliminating $\tilde{u}_0$ and $\tilde{v}_0$. The resulting equation and boundary conditions for $\tilde{p}_0$ are

$$\frac{\mathrm{d}}{\mathrm{d}\varsigma}\left(\frac{\varsigma}{\overline{\rho u}^2}\frac{\mathrm{d}\tilde{p}_0}{\mathrm{d}\varsigma}\right) - \frac{k_0^2\varsigma}{\overline{\rho u}^2}(1 - M_p^2\overline{\rho u}^2)\tilde{p}_0 = 0 \tag{27}$$

$$\varsigma = r_0 \qquad \frac{d\tilde{p}_0}{d\varsigma} = 0 \tag{28}$$

$$\varsigma \to \infty \qquad \tilde{p}_0 \to 0 \tag{29}$$

Homogeneous differential system (27–29) forms a singular Sturm–Liouville eigenvalue problem. It is singular because the range of ς is semi-infinite. The eigenvalue is k_0. For this type of problem, it is known that there are infinitely many eigenvalues and eigenfunctions. Let the jth eigenvalue and eigenfunction be denoted as k_j and $\tilde{p}_{0j}$ ($j = 1, 2, 3, \ldots$). On following standard treatment of the Sturm–Liouville problem, it is easy to show that the eigenfunctions are orthogonal with respect to a weighing function $\varsigma(M_p^2\overline{\rho u}^2 - 1)/(\overline{\rho u}^2)$, that is,

$$\int_{r_0}^{\infty}\frac{\varsigma}{\overline{\rho u}^2}(M_p^2\overline{\rho u}^2 - 1)\tilde{p}_{0i}\tilde{p}_{0j}\,\mathrm{d}\varsigma = 0, \qquad (i \neq j) \tag{30}$$

Once the jth eigenfunction $\tilde{p}_{0j}$ is found, the corresponding $\tilde{u}_{0j}$, $\tilde{v}_{0j}$ may be determined by Eqs. (24) and (25). Thus, the jth eigenvector of the shock cell Fourier mode $(\tilde{u}_0, \tilde{v}_0, \tilde{p}_0)$ may be expressed as a sum of the eigenvectors, that is,

$$\begin{bmatrix}\tilde{u}_0\\ \tilde{v}_0\\ \tilde{p}_0\end{bmatrix} = \sum_{j=1}^{\infty} Re\left\{A_j\begin{bmatrix}\tilde{u}_{0j}\\ \tilde{v}_{0j}\\ \tilde{p}_{0j}\end{bmatrix}e^{ik_{0j}\xi}\right\} \tag{31}$$

where A_j is the amplitude of the jth Fourier mode.

At the nozzle exit of the secondary jet, the pressure of the shock cell structure given by Eq. (31) must match the mismatched pressure of Eq. (6). This condition may be written as

$$\xi = 0, \qquad \Delta p[H(\varsigma - r_0) - H(\varsigma - r_0 - h)] = \sum_{j=1}^{\infty} A_j \tilde{p}_{0j} \quad (32)$$

where H( ) is the unit step function and

$$\Delta p = \left\{ \left[\frac{2}{\gamma + 1} \left(1 + \frac{\gamma - 1}{2} M_S^2 \right) \right]^{\frac{\gamma}{\gamma - 1}} - 1 \right\} \frac{1}{\gamma M_P^2}$$

By applying orthogonality conditions (30–32), it is easy to find that the Fourier mode amplitude A_j is given by

$$A_j = \frac{\Delta p \int_{r_0}^{r_0 + h} (\varsigma / \overline{\rho u}^2) \left(M_p^2 \overline{\rho u}^2 - 1 \right) \tilde{p}_{0j} \, \mathrm{d}\varsigma}{\int_{r_0}^{\infty} (\varsigma / \overline{\rho u}^2) \left(M_p^2 \overline{\rho u}^2 - 1 \right) \tilde{p}_{0j}^2 \, \mathrm{d}\varsigma_{\xi = 0}} \quad (33)$$

With A_j found, the starting conditions at $\xi = 0$ for the jth Fourier mode of the shock cell structure is known. It is equal to $Re[A_j \tilde{u}_{0j}, A_j \tilde{v}_{0j}, A_j \tilde{p}_{0j}]$.

C. Computation of the *j*th Eigenvalue and Eigenfunction

To compute the eigenvalue and eigenfunction of Eq. (27) and boundary conditions (28) and (29), we note that for large ς, that is, $\varsigma \to \infty$,

$$\bar{u} \to u_\infty, \qquad \frac{\partial \bar{u}}{\partial \varsigma} \to 0 \quad (34)$$

where u_∞ is the external freestream velocity. It is equal to zero for a jet discharged into a static environment. Thus, outside the jet at large ς, Eq. (27) reduces to

$$\frac{\mathrm{d}^2 \tilde{p}_{0j}}{\mathrm{d}\varsigma^2} + \frac{1}{\varsigma} \frac{\mathrm{d}\tilde{p}_{0j}}{\mathrm{d}\varsigma} - k_{0j}^2 \left(1 - M_p^2 \rho_\infty u_\infty^2 \right) \tilde{p}_{0j} = 0 \quad (35)$$

The solution of Eq. (35), which is bounded as $\varsigma \to \infty$, is

$$\tilde{p}_{0j} = C K_0 \left[k_{0j} \left(1 - M_p^2 \rho_\infty u_\infty^2 \right)^{\frac{1}{2}} \varsigma \right] \quad (36)$$

where $K_0[z]$ is the modified Hankel function of order zero and argument z. C is an arbitrary constant.

We will determine the eigenvalue and eigenfunction by integrating Eq. (27) numerically. To start numerical integration by a Runge–Kutta integrator, we begin at a point $\varsigma = \varsigma^*$ and integrate inward toward the nozzle. The point $\varsigma = \varsigma^*$ is located outside the jet flow. Solution (36) is used as the starting condition. Integrating in the direction toward the nozzle is important. This is because, for ς outside the jet, one solution of Eq. (27) grows exponentially as ς increases, while the other solution, given by Eq. (36), decreases exponentially. By integrating inward, the solutions have exactly the opposite behavior. In this way, as the integration proceeds, the numerical solution would not pick up the wrong solution due to round-off or other errors.

Because an eigenfunction can be determined only up to an arbitrary multiplicative constant, we may, for convenience, set $C = 1$ in Eq. (36). By means of the starting condition Eq. (36) at $\varsigma = \varsigma^*$, Eq. (27) is integrated numerically until the point $\varsigma = r_0$ is reached. The boundary condition at $\varsigma = r_0$ is $\mathrm{d}\tilde{p}_{0j}/\mathrm{d}\varsigma = 0$. This condition is, in general, not satisfied unless k_{0j} is set equal to an eigenvalue. This is done by adjusting the value of k_{0j} iteratively, say, using Newton's iteration. A iterative scheme, however, would require a good initial starting eigenvalue. For the lowest few eigenvalues ($j = 1, 2, 3, \ldots$), we may make use of the shock cell spacing found by the full shock cell structure computation discussed in the previous section. Suppose the shock cell spacing is λ. We recommend the use of the following starting wave numbers:

$$k_{01} = 2\pi/\lambda, \qquad k_{02} = 4\pi/\lambda, \qquad k_{03} = 6\pi/\lambda, \quad \text{etc.}$$

One may stop the iteration process once it is found that the desired accuracy is attained. In this way, the Fourier modes of a shock cell structure can be computed systematically.

V. Numerical Results and Comparisons with Experiments

This study is a part of Boeing's broadband shock cell noise project. In addition to the present work, a parallel experimental program is carried out at the Boeing anechoic facility. Extensive broadband shock cell noise data are measured. Details of the test program and preliminary experimental results may be found in Viswanathan [32]. Some of the measured data will be used to compare with our numerical results. All the numerical results reported here are for a nozzle with a cross section configuration and dimensions as shown in Fig. 1. This is the nozzle configuration used in the experiment.

A. Pressure Contours of Shock Cell Structure

A computer program that computes the shock cell structure as discussed in Sec. III has been developed. By means of this program, all the variables associated with a shock cell structure may be calculated for a specified jet operating condition. Figure 6 shows the computed pressure contours of the shock cell structure of a jet with $M_p = 0.72$, $T_p^{(r)}/T_a = 2.14$, $M_s = 1.36$, and $T_s^{(r)}/T_a = 1.0$. The dotted line in this figure is the lip line of the secondary jet. The contour pattern suggests that, for this jet operating condition, the shock cells are fairly regularly spaced in the region between the nozzle exits of the secondary and primary jets. The shocks and expansion fans in this region are reflected back into the supersonic jet stream by the outside mixing layer and the nozzle wall. As pointed out by Tam et al. [25], the shock cell structure is literally waves and disturbances trapped inside the jet. Downstream of the primary jet, the shock cells become highly irregular. The reason appears to be that

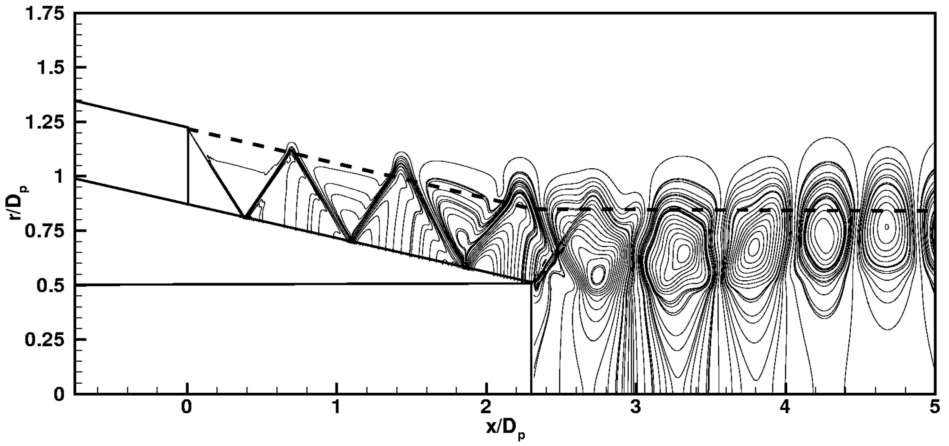

Fig. 6 Pressure contours of the shock cell structure of a dual-stream jet with $M_p = 0.72$, $T_p^{(r)}/T_a = 2.14$, $M_s = 1.36$, and $T_s^{(r)}/T_a = 1.0$. Dotted line is the lip line of the secondary jet.

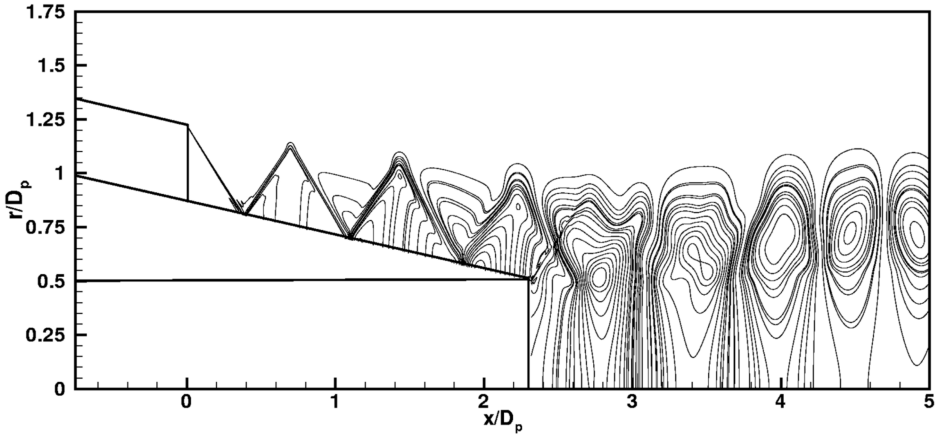

Fig. 7 Pressure contours of the shock cell structure of a dual-stream jet with $M_p = 0.85$, $T_p^{(r)}/T_a = 2.26$, $M_s = 1.36$, and $T_s^{(r)}/T_a = 1.0$.

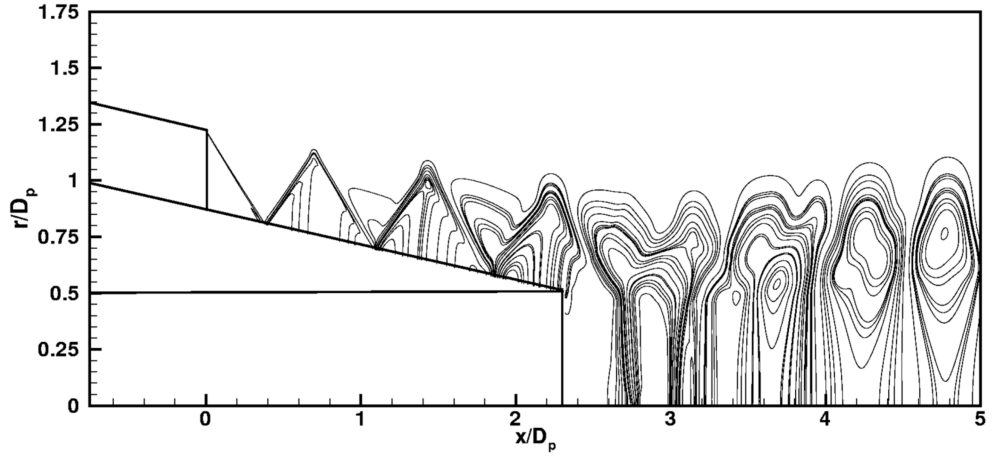

Fig. 8 Pressure contours of the shock cell structure of a dual-stream jet with $M_p = 0.96$, $T_p^{(r)}/T_a = 2.37$, $M_s = 1.36$, and $T_s^{(r)}/T_a = 1.0$.

a shock is induced at the lip of the primary nozzle. This shock initiates a second shock cell system. The superposition of two shock cell systems creates an extremely irregular pattern, even though each system by itself is quasi periodic.

Figure 7 shows the shock cell pressure contours for a jet similar to that of Fig. 6. The main difference is that the Mach number of the primary jet is increased to 0.85. It is easy to observe that by increasing the Mach number of the primary jet, the shock initiated at the lip of the primary nozzle becomes quite weak. Figure 8 shows the pressure contours pattern of the jet when the Mach number of the primary jet is further increased to 0.96, just below supersonic. In this case, there is no primary jet nozzle lip induced shock. The regular shock cell pattern extends much farther downstream.

B. Fourier Modes of Shock Cell Structure

In the previous section, the methodology to compute Fourier modes of a shock cell structure is discussed at length. Here, we will report some numerical results computed according to this method. The full line in Fig. 9 shows the distribution of shock cell pressure along the lip line of the secondary jet (see Fig. 6). The jet operating condition is the same as in Fig. 6. The pressure distribution is taken from the same numerical results. The distance from the nozzle exit measured along the lip line is ξ. The dotted line is the combined pressure of the first four Fourier modes. As can be seen, there is good agreement between the shock cell structure computation result and that by computing individual Fourier modes. Figure 10 provides a more detailed comparison. Figure 10a is the static pressure distribution of the first Fourier mode. Figures 10b–10d are the pressure distributions of the second, third, and fourth Fourier modes. It is clear that, as the mode number increases, the amplitude as well as the local wavelength decrease rapidly. Figure 10e displays again the comparison between the result of direct shock cell computation and the sum of the contributions from the first four Fourier modes. Note that the pressure distributions of the Fourier modes are not sinusoidal. This is the direct consequence of the rather drastic change in the mean flow in the proximity of the primary jet nozzle exit.

Figure 11 shows the pressure distribution along the lip line for a dual-stream jet operating at $M_p = 0.96$, $T_p^{(r)}/T_a = 2.37$, $M_s = 1.36$, and $T_s^{(r)}/T_a = 1.0$. The pressure contours of this jet are shown in Fig. 8. Figures 11a–11d are the pressure distributions of the first four Fourier modes. By comparing Figs. 10a and 11a, it is clear that changing the Mach number of the primary jet does influence the shock cell spacing and amplitude. It is seen that, at a primary jet Mach number closer to unity, the shock cell spacings are wider. Figure 11e shows a comparison between the pressure distribution from direct numerical solution of the shock cell structure and that by summing the contributions of the first four Fourier modes. There is clearly good agreement.

C. Wave Number Spectrum

It is obvious from Figs. 9–11 that the pressure distribution along the lip line of the secondary jet of each Fourier mode is not sinusoidal. In other words, it is not of a single wave number. This is not unexpected. The basic reasons are the divergence of the mean flow in the downstream direction and the complexity of the shock cell structure in the proximity of the exit of the primary nozzle. To determine the principal wave number of a shock cell structure, we apply fast Fourier transform to the pressure distribution of each Fourier mode along the lip line. Figure 12 shows the wave number spectra, absolute value of the Fourier transform, of the pressure distributions along the lip line ($0 \le x/D_p \le 11$) of the first and second Fourier mode. The dual-stream jet operating conditions are

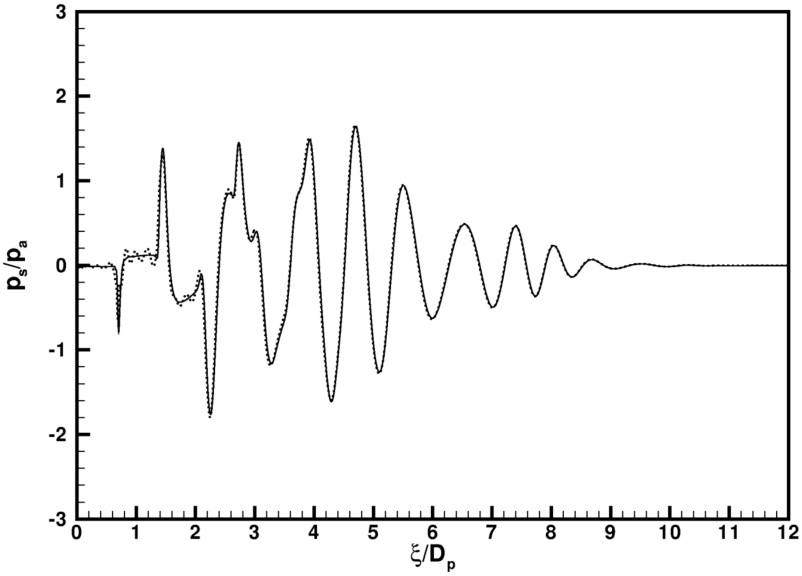

Fig. 9 Shock cell static pressure distribution along the lip line of the secondary jet. Jet operating condition is the same as Fig. 6. Solid line is measured from Fig. 6; dotted line is the first four Fourier modes.

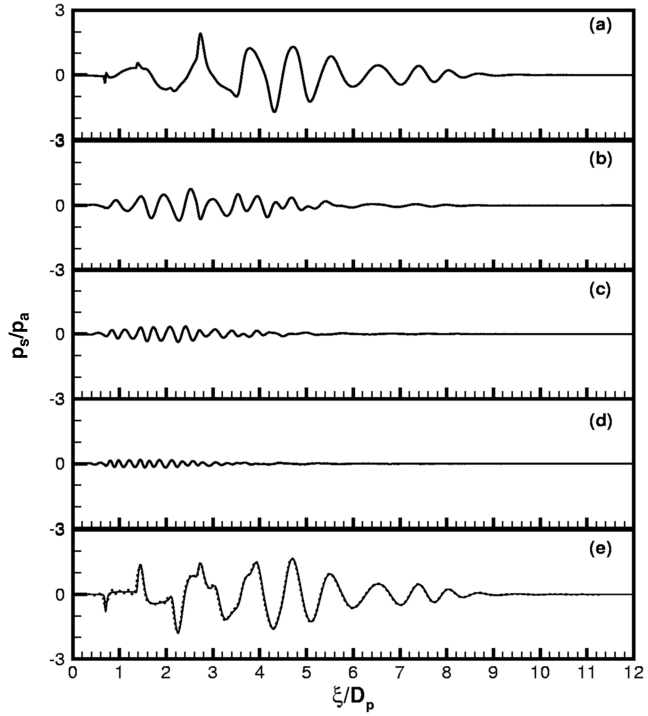

Fig. 10 Static pressure distribution of shock cell structure along the lip line of the secondary jet. Jet operating condition is the same as Fig. 6: a–d) first, second, third, and fourth Fourier modes; e) full line is from data of Fig. 6, dotted line is the sum of the first four modes.

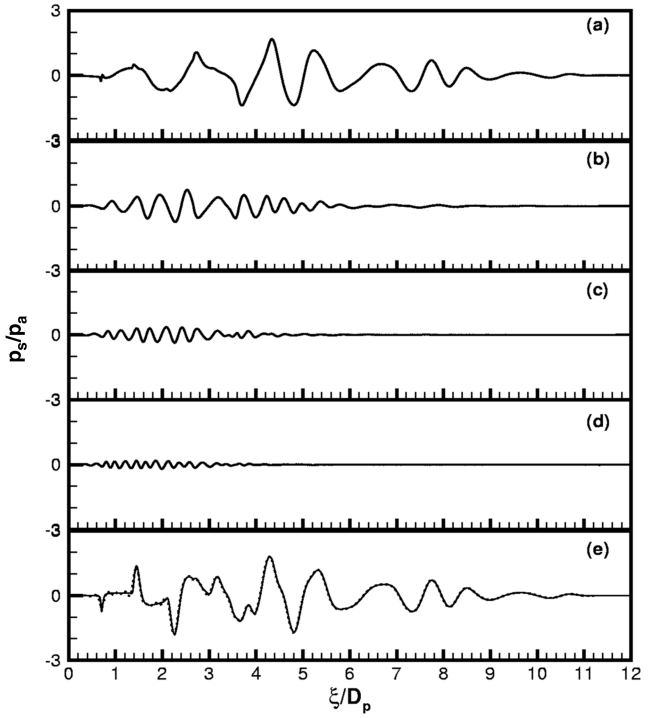

Fig. 11 Static pressure distribution of shock cell structure along the lip line of the secondary jet. Jet operating condition is the same as Fig. 8: a–d) first, second, third, and fourth Fourier modes; e) full line is from data of Fig. 8, dotted line is the sum of the first four modes.

the same as in Fig. 6. The full line is the spectrum of the first mode. The spectrum peaks at $k_1 D_p/(2\pi) = 1.13$. The dotted line is the spectrum of the second Fourier mode. The spectrum peaks at $k_2 D_p/(2\pi) = 2.0$. Thus, we may consider the wave number of the fundamental mode to be $k_1 D_p/2\pi = 1.13$ and the wave number of the second mode to be $k_2 D_p/2\pi = 2.0$. Figure 13 is the wave number distribution of the first Fourier mode of a jet operating at $M_p = 0.85$, $T_p^{(r)}/T_a = 2.26$, $M_s = 1.28$, and $T_s^{(r)}/T_a = 1.0$ measured along the lip line ($0 \le x/D_p \le 11$). The spectrum peaks at $k_1 D_p/2\pi = 1.2$.

We would like to remark that it is possible to perform a wave number spectrum analysis on the pressure distribution of the entire shock cell structure. However, because of the complexity of the shock cells, the resulting spectrum consists of numerous closely spaced peaks. This makes it somewhat difficult to clearly identify the wave numbers of the fundamental and the secondary mode. On the other hand, the use of Fourier modes and the restriction of the Fourier transform to only the noise producing region of the jet allow an unambiguous identification.

D. Comparisons with Experimental Measurements

Equation (16) provides a relationship between the frequency at the jth peak of the broadband shock cell noise spectrum (we shall call this frequency the peak frequency) in direction θ without forward

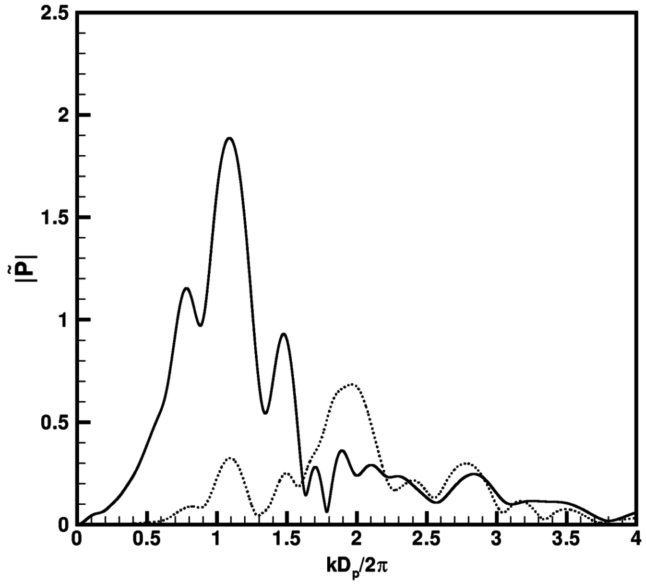

Fig. 12 Wave number spectra of a jet with operating condition as in Fig. 6. Full line is the spectrum of the first Fourier mode. Dotted line is the spectrum of the second Fourier mode.

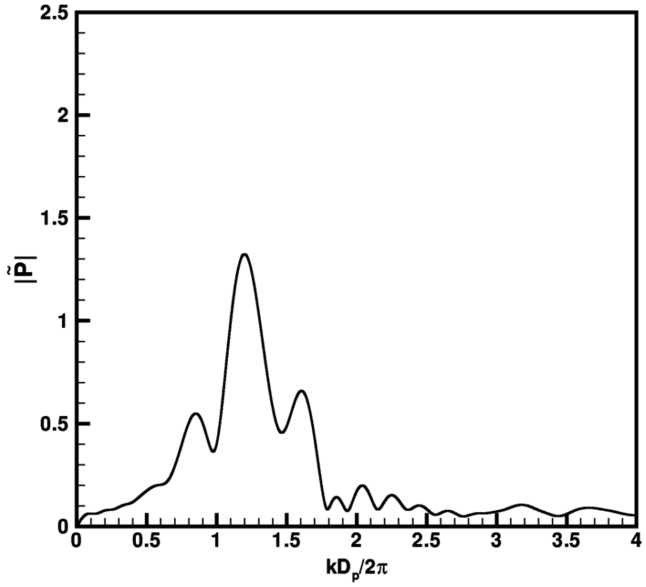

Fig. 13 Wave number spectra of a jet at $M_p = 0.85$, $T_p^{(r)}/T_a = 2.26$, $M_s = 1.28$, and $T_s^{(r)}/T_a = 1.0$. Full line is the spectrum of the first Fourier mode.

flight. We may use this formula to calculate the peak frequencies if k_j and u_c are known. For cold jets at moderate supersonic Mach number, Tam et al. [3,9,10] have demonstrated that convection velocity u_c may be taken as 0.7 times the fully expanded jet velocity. Thus, if we insert the computed values of $k_1, k_2, \ldots$ into Eq. (16), it becomes possible to calculate the peak frequencies. The accuracy of the prediction can be established by comparison with experimental measurements. Good agreement would be an indication that the computational methodology is valid and the computed shock cell structure is accurate.

Figure 14 shows the measured noise spectra of a dual-stream jet operating at $M_p = 0.72$, $T_p^{(r)}/T_a = 2.14$, $M_s = 1.36$, and $T_s^{(r)}/T_a = 1.0$ at inlet angle 50, 70, 90, and 100 deg. The high-frequency part of the noise spectra, to the right of the screech tone at nearly the center of the spectra, is dominated by two broadband shock cell noise peaks. The two arrows in each of the noise spectra are the peak frequencies calculated by Eq. (16). The two wave numbers, $k_1 D_p/2\pi$ and

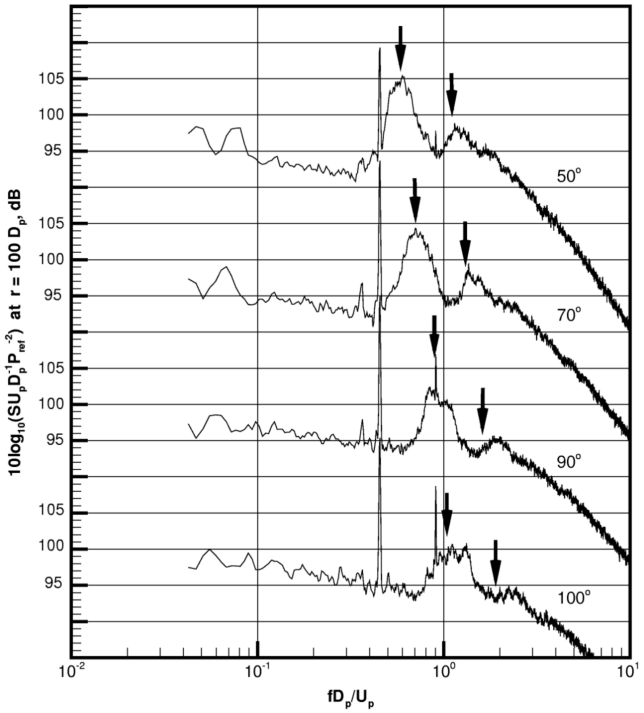

Fig. 14 Broadband shock cell noise spectrum at inlet angle 50, 70, 90, and 100 deg; $M_p = 0.72$, $T_p^{(r)}/T_a = 2.14$, $M_s = 1.36$, and $T_s^{(r)}/T_a = 1.0$; $k_1 D_p/2\pi = 1.13$, $k_2 D_p/2\pi = 2.0$. Arrows indicate the computed peak frequencies.

$k_2 D_p/2\pi$, used in the calculation are taken from Fig. 12. They are 1.13 and 2.0, respectively. As can be seen, there is good agreement between the predictions of Eq. (16) and measured data. Figure 15 shows similar comparisons between peak frequencies computed and experimental spectral measurements. For this jet at $M_p = 0.85$, $T_p^{(r)}/T_a = 2.26$, $M_s = 1.28$, and $T_s^{(r)}/T_a = 1.0$, there is one prominent broadband shock cell noise peak. The computed $k_1 D_p/2\pi$ is 1.20 (see Fig. 13). Again, the arrows indicate the computed peak noise frequencies. Finally, Fig. 16 offers a further example on the accuracy of Eq. (16). It is easy to see that, again, there is good agreement between predictions and experimental measurements. The good agreements in the cases reported and in the many cases unreported (because of space limitation) strongly suggest that the shock cell structure must have been accurately computed.

VI. Conclusions

Broadband shock cell noise is an important interior noise problem for present-day commercial aircraft at cruise condition. Shock cell noise is generated by the interaction of the large turbulence structures of the jet flow and the quasi-periodic shock cells in the jet plume. In this work, the shock cell structure of a modern commercial aircraft jet engine is computed using a linear model. The shock cells in the supersonic secondary jet is generated primarily by the pressure mismatch at the nozzle exit. The methodology of the present work is to compute first the pressure mismatch at the nozzle exit. The shock cell structure is then determined computationally by solving the linearized RANS equations, satisfying the pressure mismatch condition at the nozzle exit of the secondary jet.

Broadband shock cell noise may be regarded as the result of coherent scattering of the large turbulence structures by the shock cells as the former propagate downstream through the latter. Coherent scattering leads to strong directional radiation. For this reason, it is the spatially periodic components of the shock cell structure that are most relevant to shock cell noise prediction. Here, because of the complexity of the shock cell structure, the periodic components are found by computing the Fourier modes of the shock cell structure. The wave number spectrum of each Fourier mode in

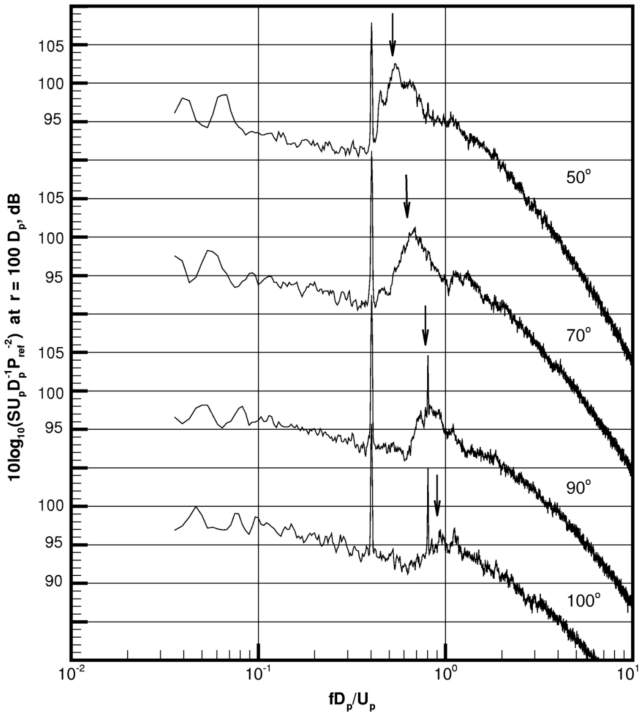

Fig. 15 Broadband shock cell noise spectrum at inlet angle 50, 70, 90, and 100 deg; $M_p = 0.85$, $T_p^{(r)}/T_a = 2.26$, $M_s = 1.28$, and $T_s^{(r)}/T_a = 1.0$; $k_1 D_p/2\pi = 1.20$. Arrows indicate the computed peak frequencies.

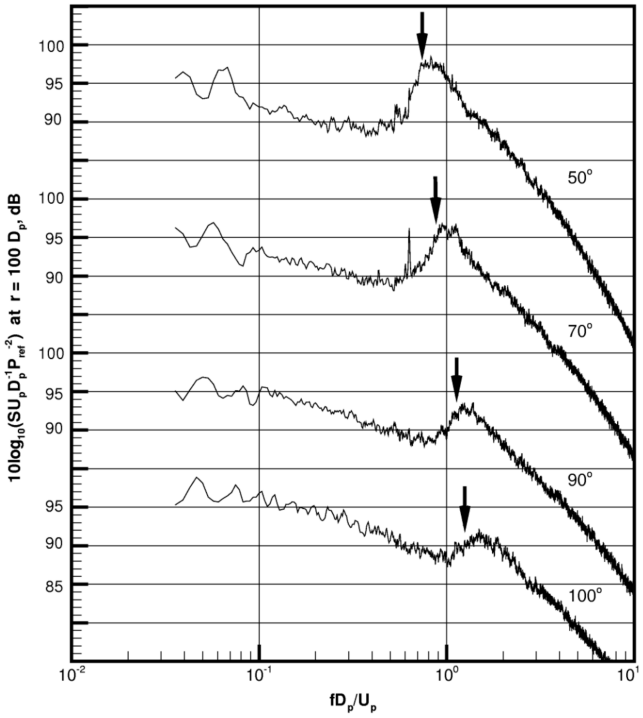

Fig. 16 Broadband shock cell noise spectrum at inlet angle 50, 70, 90, and 100 deg; $M_p = 0.85$, $T_p^{(r)}/T_a = 2.26$, $M_s = 1.19$, and $T_s^{(r)}/T_a = 1.0$; $k_1 D_p/2\pi = 1.76$. Arrows indicate the computed peak frequencies.

the shock cell noise producing region of the jet is then computed to identify the dominant spatially periodic components. The applicability of this approach is validated by using the dominant wave number found to calculate the frequencies at the peaks of experimentally measured broadband shock cell noise spectra. Good agreements are found over a range of primary and secondary jet Mach numbers. Finally, we want to make it known that we are aware that computation of the shock cell structure is but the first step in the development of a shock cell noise prediction method/theory. Work is now underway toward this goal.

Acknowledgments

The work of C. Tam and N. Pastouchenko was supported by a contract from The Boeing Company. Krishna Viswanathan is the Technical Monitor and the Boeing Principal Investigator for the project.

References

[1] Harper-Bourne, M., and Fisher, M. J., "The Noise from Shockwaves in Supersonic Jets," *Proceedings (No. 131) of the AGARD Conference on Noise Mechanisms*, AGARD Paper No. 1311973.

[2] Tanna, H. K., "An Experimental Study of Jet Noise, Part II: Shock Associated Noise," *Journal of Sound and Vibration*, Vol. 50, No. 3, 1977, pp. 429–444. doi:10.1016/0022-460X(77)90494-1

[3] Tam, C. K. W., and Tanna, H. K., "Shock Associated Noise of Supersonic Jets from Convergent-Divergent Nozzles," *Journal of Sound and Vibration*, Vol. 81, No. 3, 1982, pp. 337–358. doi:10.1016/0022-460X(82)90244-9

[4] Norum, T. D., and Seiner, J. M., "Measurements of Mean Static Pressure and Far Field Acoustics of Shock-Containing Supersonic Jets," NASA TM 84521d, 1982.

[5] Norum, T. D., and Shearin, J. G., "Effects of Simulated Forward Flight on the Structure and Noise of an Underexpanded Jet," NASA TP-2308, 1984.

[6] Norum, T. D., and Shearin, J. G., "Shock Structure and Noise of Supersonic Jets in Simulated Flight to Mach 0.4," NASA TP-2785, 1988.

[7] Norum, T. D., and Brown, M. C., "Simulated High Speed Flight Effects on Supersonic Jet Noise," AIAA Paper 93-4388, 1993.

[8] Brown, W. H., Ahuja, K. K., and Tam, C. K. W., "High Speed Flight Effects on Shock Associated Noise," AIAA Paper 86-1944, 1986.

[9] Tam, C. K. W., Seiner, J. M., and Yu, J. C., "Proposed Relationship Between Broadband Shock Associated Noise and Screech Tones," *Journal of Sound and Vibration*, Vol. 110, No. 2, 1986, pp. 309–321. doi:10.1016/S0022-460X(86)80212-7

[10] Tam, C. K. W., "Stochastic Model Theory of Broadband Shock Associated Noise from Supersonic Jets," *Journal of Sound and Vibration*, Vol. 116, No. 2, 1987, pp. 265–302.

[11] Tam, C. K. W., "Broadband Shock Associated Noise of Moderately Imperfectly Expanded Supersonic Jets," *Journal of Sound and Vibration*, Vol. 140, No. 1, 1990, pp. 55–71. doi:10.1016/0022-460X(90)90906-G

[12] Tam, C. K. W., "Broadband Shock-Associated Noise from Supersonic Jets in Flight," *Journal of Sound and Vibration*, Vol. 151, No. 1, 1991, pp. 131–147. doi:10.1016/0022-460X(91)90656-5

[13] Tam, C. K. W., "Broadband Shock Associated Noise from Supersonic Jets Measured by a Ground Observer," *AIAA Journal*, Vol. 30, No. 10, 1992, pp. 2395–2401. doi:10.2514/3.11239

[14] Lui, C., and Lele, S. K., "Sound Generation Mechanism of Shock-Associated Noise," AIAA Paper 2003-3315, May 2003.

[15] Lele, S. K., "Phased Array Models of Shock-Cell Noise Sources," AIAA Paper 2005-2841, May 2005.

[16] Bodony, D. J., Ryu, J., and Lele, S. K., "Investigating Broadband Shock-Associated Noise of Axisymmetric Jet Using Large Eddy Simulation," AIAA Paper 2006-2495, May 2006.

[17] Tanna, H. K., Tam, C. K. W., and Brown, W. H., "Shock-Associated Noise of Inverted Profile Coannular Jets: Part I: Experiments, Part II: Conditions for Minimum Noise, Part III: Shock Structures and Noise Characteristics," *Journal of Sound and Vibration*, Vol. 98, No. 1, 1985, pp. 95–145. doi:10.1016/0022-460X(85)90405-5

[18] Long, D. F., "The Structure of Shock Cell Noise from Supersonic Jets," AIAA Paper 2005-2841, May 2005.

[19] Long, D. F., "Effect of Nozzle Geometry on Turbofan Shock Cell Noise at Cruise," AIAA Paper 2005-0998, Jan. 2005.

[20] Harper-Bourne, M., and Wrighton, C., "The Design, Development and Commissioning of a Test Capability for Studying Cruise Noise," AIAA Paper 2005-3051, May 2005.

[21] Abdelhamid, Y. A., and Ganz, U. W., "Prediction of Shock-Cell Structure and Noise in Dual Stream Flow Nozzles," AIAA Paper 2007-3721, May 2007.

[22] Rask, O. H., Gutmark, E. J., and Martens, S., "Broadband Shock Associated Noise Suppression by Chevrons," AIAA Paper 2006-0009, Jan. 2006.
[23] Rask, O. H., Gutmark, E. J., and Martens, S., "Shock Cell Modification due to Chevrons," AIAA Paper 2007-0831, Jan. 2007.
[24] Gutmark, E. J., Rask, O. H., and Michel, U., "How Chevrons Decrease Broadband Jet Noise in Cruise," AIAA Paper 2007-3611, May 2007.
[25] Tam, C. K. W., Jackson, J. A., and Seiner, J. M., "A Multiple-Scales Model of the Shock-Cell Structure of Imperfectly Expanded Supersonic Jets," *Journal of Fluid Mechanics*, Vol. 153, No. 2, 1985, pp. 123–149. doi:10.1017/S0022112085001173
[26] Tam, C. K. W., and Pastouchenko, N. N., "Fine-Scale Turbulence Noise from Dual Stream Jets," *AIAA Journal*, Vol. 44, No. 1, 2006, pp. 90–101. doi:10.2514/1.18018
[27] Tam, C. K. W., and Webb, J. C., "Dispersion-Relation-Preserving Finite Difference Scheme for Computational Acoustics," *Journal of Computational Physics*, Vol. 107, No. 2, 1993, pp. 262–281. doi:10.1006/jcph.1993.1142
[28] Tam, C. K. W., and Kurbatskii, K. A., "Multi-Size-Mesh Multi-Time-Step Dispersion-Relation-Preserving Scheme for Multiple Scales Aeroacoustics Problems," *International Journal of Computational Fluid Dynamics*, Vol. 17, No. 2, 2003, pp. 119–132. doi:10.1080/1061856031000104860
[29] Tam, C. K. W., and Dong, Z., "Wall Boundary Conditions for High Order Finite Difference Schemes in Computational Aeroacoustics," *Theoretical and Computational Fluid Dynamics*, Vol. 6, Nos. 5–6, 1994, pp. 303–322. doi:10.1007/BF00311843
[30] Shen, H., and Tam, C. K. W., "Three-Dimensional Simulation of the Screech Phenomenon," *AIAA Journal*, Vol. 40, No. 1, 2002, pp. 33–41. doi:10.2514/2.1638
[31] Pack, D. C., "A Note on Prandtl's Formula for the Wave Length of a Supersonic Gas Jet," *Quarterly Journal of Mechanics and Applied Mathematics*, Vol. 3, No. 2, 1950, pp. 173–181. doi:10.1093/qjmam/3.2.173
[32] Viswanathan, K., "Parametric Study of Noise from Dual-Stream Nozzles," *Journal of Fluid Mechanics*, Vol. 521, Dec. 2004, pp. 35–68. doi:10.1017/S0022112004000813

C. Bailly
Associate Editor